Powder Technology 452 (2025) 120566

Contents lists available at ScienceDirect

Powder Technology

journal homepage: www.journals.elsevier.com/powder-technology

Coupled numerical simulation of the drying and calendering for Lithium-ion battery anodes with non-spherical particles

Mark Lippke [a], Caroline Willuhn [a,*], Tobias Ohnimus [a], Thilo Heckmann [b], Philip Scharfer [b], Wilhelm Schabel [b], Carsten Schilde [a], Arno Kwade [a]

[a] Institute for Particle Technology, Technische Universität Braunschweig, Volkmaroder Str.5, 38104 Braunschweig, Germany
[b] Thin Film Technology (TFT), Karlsruhe Institute of Technology (KIT), 76131 Karlsruhe, Germany

HIGHLIGHTS

- Coupling of different modeling techniques for anode production.
- Approach that covers kinetics, structure formation and binder migration.
- Explicit consideration of particle shapes on calendering behavior.

GRAPHICAL ABSTRACT

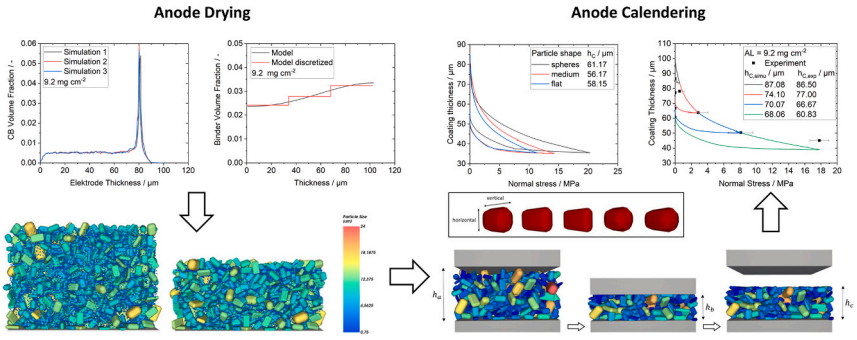

ARTICLE INFO

Keywords:
Battery
Drying
Calendering
Electrode
DEM
Microstructure simulation

ABSTRACT

As the drying and calendering processes are crucial to the resulting electrode microstructure and, therefore, electrode performance, various approaches have been developed for modeling these two processes.

In this work, the drying and calendering processes of graphite anodes were modeled using the Discrete Element Method to predict the anode microstructure, inactive material distribution and final film thickness. The drying model comprised a drying-kinetic model, a binder model, and a structure-oriented model. Calendering was modeled using anode structures obtained from the drying model. Although drying and calendering has been modeled for spherical cathode active materials, the modeling of irregular graphite particles is much more challenging.

Unprecedentedly, in this study, the flake-like shape of the graphite particles was considered. While the drying model was able to accurately predict coating thickness and porosity, the calendering model was able to reproduce experimental calendering results up to a moderate degree of compaction.

Finally, the deformation behavior of graphite anodes was investigated experimentally. It was found that beyond a certain calendering stress of approximately 5 MPa, further anode deformation is completely plastic. This was identified as the reason for the calendering model limitations. Ideas for contact model modifications were suggested.

* Corresponding author.
E-mail address: c.willuhn@tu-braunschweig.de (C. Willuhn).

https://doi.org/10.1016/j.powtec.2024.120566
Received 29 October 2024; Received in revised form 29 November 2024; Accepted 13 December 2024
Available online 17 December 2024

1. Introduction

It is expected that the worldwide Lithium-ion battery (LIB) demand will grow by nearly 27 % annually and reach 4,7 TWh by 2030 [1]. More than 90 % of this accumulated power will be needed for mobility applications, followed by stationary storage and consumer electronics. To cope with the demand, LIB performance needs to be optimized, which can be achieved by dedicating attention to each process step along the fabrication chain. Thorough analysis of the interaction between all manufacturing steps is obligatory to optimize their interactions and to achieve the best cell performance possible [2].

Two highly influential process steps in Li-ion cell fabrication are drying and calendering of the electrode coating. Both are pivotal steps regarding the formation of the electrode microstructure, including its porosity, material distribution and mechanical stability.

Electrode drying directly follows the coating of the electrode slurry on the current collector. Ideally, it should remove the solvent used for dispersing the dry materials as fast and efficiently as possible. However, high drying speeds decrease electrode quality, as the binder accumulates on the surface [3,4]. This not only lowers adhesion to the current collector, but also reduces overall electrode performance.

As a next step, the dried electrodes are calendered. Being a compaction process, calendering reduces the microstructure's porosity, which increases particle contacts, so that electronically conductive agents form contiguous networks, improving the electronic conductivity of the electrodes [5,6]. Electrode calendering also contributes to the mechanical integrity of the cell, ensuring that the electrodes remain intact and securely bound to the current collectors [7–9]. However, lower electrode porosities also diminish the accessibility of lithium ions to the active materials during charge and discharge cycles [6]. An optimal calendering degree achieves enhanced electrical conductivity and mechanical stability at sufficient ion mobility [10].

Various approaches exist for the numerical modeling of microstructure formation during electrode drying. Most of them are based on the discrete element method or on the closely related coarse-grained molecular dynamics (CGMD). In both simulation methods, precise distinction must be made between carbon black and binder, as well as the solvent.

A first approach by Srivastava [11] combines carbon black and binder to form clustered (coarse grained) so-called carbon black binder domain particles (CBD particles). The surrounding solvent is imprinted on the particles by viscous forces. Adhesive forces between the particles are described by the John-son-Kendall-Roberts model (JKR model). The evaporation of the solvent is represented by compressing the simulation domain from above to a target layer thickness. The model of Srivastava et al. focuses on using the derived structures to make statements about electrical conductivity and tortuosity as a function of the adhesion forces between the CBD particles and the active material particles. The model was not used to predict layer thickness or porosity after either drying or calendering.

The CGMD-based drying model by Lombardo et al. [12,13] also uses substitute spherical CBD particles. However, these also contain solvent, which is why these particles shrink during the drying process in order to model the evaporation of the solvent. By applying a constant pressure corresponding to the ambient pressure to the simulation domain, the layer shrinks together. The Lennard-Jones potentials commonly used in molecular dynamics act between the particles and have been calibrated in such a way that the rheological behavior of the slurry could be simulated in a simulated shear cell [12]. During drying, the domain is divided into three equal segments along the layer thickness, in which the CBD particles shrink at different rates. The closer the respective segment is located to the electrode‘s surface, the faster the CBD particles shrink in order to represent faster drying in the higher layers of the electrode. The CBD particles in the upper area receive higher attractive forces in order to represent the capillary suction causing binder segregation. By evaluating the local distribution of the CBD particles at the end of the simulation at different drying rates, it was possible to show effects such as the sensitivity of different drying phases with regard to binder segregation as a result of different drying rates.

Since the slurry serves as the input for the drying process, it largely influences the drying results. Previous studies by Lombardo et al. were successful at depicting the experimental slurry behavior using force fields [12,14]. In this study, the interactions within the slurry is represented as the sum of particle interactions, modeled based on literature. Lippke et al. developed a DEM-based drying approach, which maps fluid effects via surrogate models and directly maps the carbon black (CB) in addition to the active material by means of coarse-graining. This enabled them to predict the layer thickness and porosity of cathodes. Details can be found in Section 2.3 and [15]. For the simulation of the drying process a model for the drying kinetics was applied, which Kumberg et al. [16,17] have developed based on energy and mass balances. The method is able to predict the drying rate, the film temperature and the residual solvent content during the drying process of LIBs. A detailed description of the model can be found in Section 2.3.1.

To predict the binder distribution during drying, in addition to the previously mentioned approach by Lombardo [13], there is also the approach by Font [18], which models the binder distribution using a convection-diffusion equation. The binder distribution along the layer thickness is described in an analytical 1D model. One point of criticism is that in Font's model, the binder transport ends when the final layer thickness is reached. This point was adressed by Zihrul et al. [19] Details can be found Section 2.3.2 and [15].

Besides drying of LIB electrodes, numerous methods have been proposed to model the process of calendering, most of them studying the cathode, as calendering the cathode improves the battery performance to a greater extent than calendering the anode [6]. Furthermore, cathode active materials are spherical, making the simulation of such materials easier and less time consuming. The different simulation approaches vary in the chosen contact model for force calculation between particles and the model's validation, as well as the choice of parameters and the method of representing the CBD.

Srivastava el al [11]. stochastically generated an electrode structure with two different particle types representing either the active material or the CBD, assuming that the binder fully agglomerates with the carbon nanoparticles. Schreiner et al. [20] also created a particle bed of active material particles by randomly positioning particles into a simulation box. The CBD was represented by a method of parallel bonding [21]. The chosen contact model was the Edinburgh Elasto-Plastic Adhesion (EEPA) [22], which not only accounted for the elastic, but also the plastic deformation of the NMC particles during compression. By adjusting bond parameters, friction and surface energy, the authors were able to recreate experimentally obtained nanoindentation curves of NCM-based cathodes. Ngandjong et al. [23] went one step further and used electrode mesostructures obtained from experimentally validated drying simulations as their calendering input structures. They used the Hertz-Mindlin model for force calculations between the active material particles, while the simplified Johnson-Kendall-Roberts model described the adhesive forces representing the adhesive nature of the binder. Sangros et al. [24,25] also modeled the AM particles as spheres and the CBD as solid bridges, but used the Thornton-Ning Model [26,27] to describe contact forces between AM particles. This decision was made based on nanoindentation results: the load-displacement curves of indentation for a single NMC particle showed that the commonly used Hertz model overestimates the mechanical behavior of NMC particles. Under low levels of compaction, the behavior of NMC is primarily elastic, which is in perfect agreement with the Hertz theory. At higher compaction, however, plastic deformation becomes important, so they cannot be modeled by the Hertz model anymore. As the Thornton-Ning Model directly accounts for such a point of transition from elastic to plastic deformation, it was chosen for the calendering simulation. The point at which the plastic particle behavior cannot be disregarded anymore is called the yield point. This experimentally derived yield

point was utilized by Sangrós et al. to parameterize their contact model. The software employed for the simulations was LIGGGHTS, where the initial calendering structure was stochastically generated. In contrast to Ngandjong et al. and Srivastava el al., whose CBD was modeled by monodisperse particles. Sangrós et al. adapted the size of the solid bridges to the respective size of particles they were attached to, and therefore enabled the modeling of a polydisperse CBD. Although the exact position of the electrochemically inactive CBD particles is not fully resolved when using the bond model to represent them, our preliminary studies using the bond model showed major advantages that arise from faster simulations and the possibility of larger representative volume elements. Forces that discrete particles would exhibit within the electrode simulation are also exhibited by the bond forces. As bonds also transfer momentum, they offer the advantage of replicating the high glue-like effect that binders are designed to have. However, the non-depiction of the inactive materials' position, i.e. the carbon black and binder particle positions, would result in a loss of accuracy in potential electrochemical simulation based on this approach.

Except Schreiner et al., who numerically investigated the calendering process by compressing the particulate microstructure using the geometry of a roll [20], all the mentioned calendering simulations placed the created particle beds between two plates, where the upper plate moved down on the microstructure to compress it.

The work done for this paper links the processes of drying and calendering of graphite anodes in two ways, thereby achieving an important step in the establishment of a digital twin for anode production. The CB and binder distribution along the film thickness received from drying simulations are directly transferred to the calendering simulation by implementing gradients in the bond volume. Furthermore, the microstructure resulting from the drying process serves as input for the particle bed for the calendering structure. Connected drying and calendering simulations have previously been reported for NMC-based cathodes [11,15,23,28]. This study presents the novelty of modeling the drying and calendering of graphite anodes, which additionally comprises the difficulty of representing the flake-like graphite particles in their realistic shape. Some studies for calendering and subsequent electronic and ionic conductivity analysis [28,29] include non-spherical particles in their electrode models that are derived from X-ray Computed Tomography scans. They conducted calendering experiments by replacing the location of their derived particles by many spherical particles, which also allowed for particle deformation and cracking. In this study, the irregular shape of the graphite particles is directly modeled by using irregular shaped model particles.

2. Materials and methods

2.1. Experimental section

The anode slurry comprises commercial graphite as the active material, two binders, namely carboxymethyl cellulose and styrene butadiene rubber, as well as CB as conductive agent (Table 1). First, the solid components are dry-mixed in the tumbling mixer TurbulaT2F (Willy A. Bachofen Corp) for 15 min at a rotational speed of 49 m min^{-1} at room temperature (RT). Then, water as a solvent is added until the solid's content amounts to 50 wt%. The slurry is dispersed in a planetary mixer (NETZSCH B.V. & Co. Holding KG) for 60 min at a circumferential speed of 9 m s^{-1}, before the SBR is added, and the suspension is degassed for 30 min at circumferential speeds of 2 m s^{-1}.

Table 1
Anode formulation.

Material	Mass Fraction
Graphite	94 wt.-%
Carboxymethyl cellulose	2 wt.-%
Styrene butadiene	3 wt.-%
Carbon black	1 wt.-%

The homogenized slurry is coated on a collector foil by a continuous coater/dryer pilot plant (LabCo, Kroenert Gmbh & Co. KG) using a comma bar process. Subsequent drying is performed in a six-meter-long dryer that is divided into three segments. All segments had a temperature of 60 °C, while the first two used indirect air flow and the last one used direct air flow to dry the anode. The drying speed was 2 m min^{-1}. Four different areal loadings (ALs) are produced, with 14.35 mg cm^{-3}, 11.35 mg cm^{-3}, 9.24 mg cm^{-3} and 7.60 g cm^{-3}. Table 2 lists the anode ALs, the porosities ϵ_E, the densities ρ_E (determined by areal weight and thickness) and the coating layer thickness d_E.

Calendering is performed on a GLK400 two-roll calender (Saueressig GmbH & Co. KG) with a roll diameter of 465 mm. Each of the four ALs were compressed to four different degrees of compaction, each defined by a certain roll gap. To directly measure the deviation of the actual roll gap to the target roll gap, the method developed by Diener et al. [30] was used. Here, the deviation $\Delta\Gamma_{gap}$ is calculated depending on the line load q_L:

$$\Delta\Gamma_{gap} = 0,061 q_L - 2,4\ \mu m \tag{1}$$

Stresses during calendering are calculated according to Meyer et al. [31], using the roll force F_r, the coating width b_{coat} and the contact length between roll and electrode k_{RE}. The latter is calculated according to Eq. (3), using the electrode thickness before and after calendering, h_a and h_c, respectively, as well as the radius of the roll r_r and the minimal roll gap h_b.

$$\sigma_r = \frac{F_r}{b_{coat} k_{RE}} \tag{2}$$

$$k_{RE} = \sqrt{R_w (h_a - h_b)} + \sqrt{R_w (h_c - h_b)} \tag{3}$$

Nanoindentation (TriboIntender TI900, Bruker Corporation) provided insights into the mechanical behavior of the manufactured anodes. Using a 50-µm flat-punch the anodes were compressed to a defined indentation depth. The force-displacement curves and the analysis of layer thickness allowed the determination of elastic and plastic components of deformation. Furthermore, scanning electron microscopy (Helios G4 CX, Thermo Fisher Scientific Inc) was carried out to visually assess the state of compaction of the anodes.

2.2. Representation of graphite particles

One focus of this work is the consideration of the non-spherical shape of the graphite particles. For this purpose, the particle model "SpheroPolygon" of the DEM code Rocky was used in the simulations. The particle shape in Rocky is defined by means of two aspect ratios and its number of corners. Five different particle templates were created per particle set (Fig. 1). Shape parameters for the particle sets "use case" and "flat" are listed in Table 3 and in the Appendix, respectively. Each particle template has four corners to reduce the computational effort.

Rocky is able to automatically adapt the size of the particles to a specified particle size distribution. For this purpose, the particle size distribution of the graphite is determined by laser diffraction (Horiba LA-960). To account for the fact that laser diffraction measurements overestimate the width of the particle size distribution, especially for non-spherical particles, and to reduce the computational effort, the upper and lower 15 % of the distribution were removed analogous to [32] (Fig. 2). Table A1 in the Appendix lists the resulting particle size distribution.

Table 2
Anode areal loadings, porosities, densities and coating layer thicknesses.

AL_E [mg cm^{-2}]	7.60 ± 0.32	9.24 ± 0.09	11.35 ± 0.09	14.35 ± 0.41
ϵ_E [%]	58.7 ± 0.57	58.11 ± 0,35	56.9 ± 0.24	56.0 ± 0.3
ρ_E [g cm^{-3}]	0.89 ± 0.01	0.9 ± 0.01	0.93 ± 0.01	0.94 ± 0.01
d_E [µm]	85.33 ± 0.55	102.3 ± 0.87	122.0 ± 0.71	151.11 ± 0.93

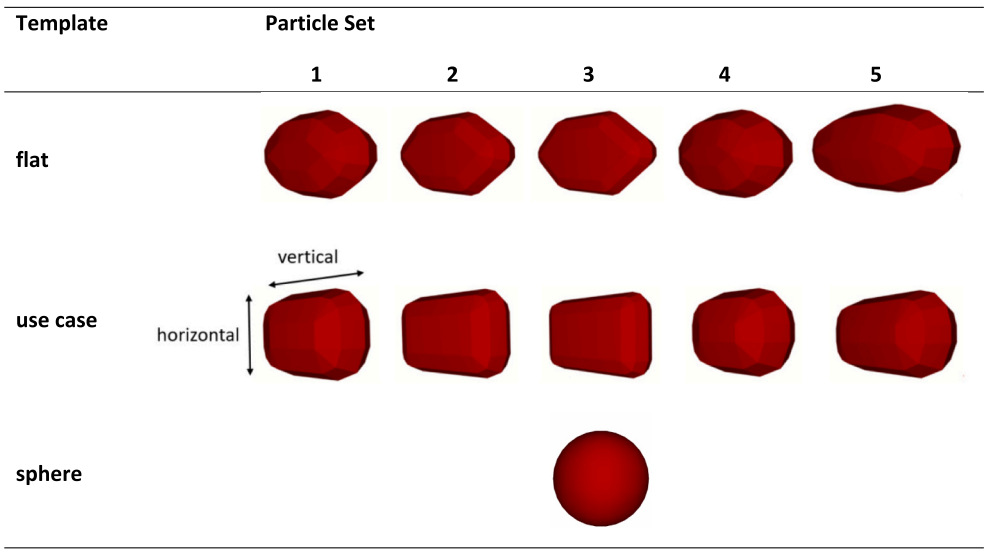

Fig. 1. Visual representation of all created particle templates for the present study. Particle set "use case" is later used for drying and calendering simulation. The set "flat" considers particles that are flatter than the "use case" particles, so that the effect of descending sphericity on the calendering simulation can later be compared. Particle templates 1–5 for the spherical particles are identical.

Table 3
Geometrical parameters of the created graphite active material particles. Vertical and horizontal direction as shown in Fig. 1.

Set: "use case"	1	2	3	4	5
Vertical aspect ratio	1.55	1.75	1.85	1.5	2.1
Horizontal aspect ratio	0.65	0.45	0.35	0.75	0.75
Number of corners*	4	4	4	4	4

* the number of corners is an input parameter set by RockyDEM to characterize non-spherical particles.

2.3. Simulation of drying step

Drying is modeled combining three approaches: The drying kinetics are modeled using the developed approach by Kumberg et al. [16], which is based on solving mass and heat balances. These predict film temperatures, drying rates, and the film shrinkage until film consolidation. The DEM-based approach presented by Lippke et al. models the formation of the electrode microstructure. The binder distribution in the course of drying is quantified by the approach of Zihrul et al. [19]

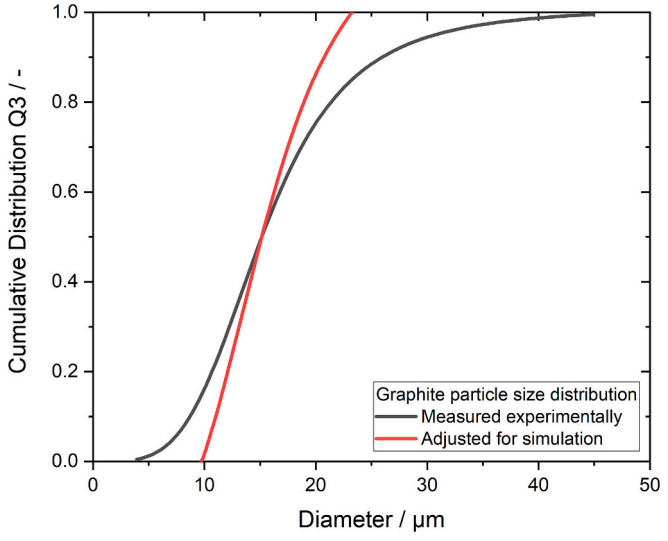

Fig. 2. Original (gray) and adjusted (red) particle size distribution of the used graphite particles. (For interpretation of the references to colour in this figure legend, the reader is referred to the web version of this article.)

2.3.1. Drying kinetics

Three phases are distinguished within the drying process. The first phase consists of a constant drying rate and constant film shrinkage rate, which both last roughly until the fluid level has reached the height of the film thickness [33–36]. If enough pores near the surface are still filled with solvent, the constant rate period can persist even after the end of film shrinkage [37]. The second phase describes a decreasing drying rate, as the remaining fluid within the electrode pores evaporates slower due to transport limitations within the pore structure, which has been observed for thick electrodes [38]. Residual moisture evaporates in the third drying phase until the electrode reaches the thermodynamic equilibrium with the surrounding atmosphere [39]. Kumberg et al. employed the following transient enthalpy balance to describe the drying [17,39]:

$$\frac{dH_{film}}{dt} = \dot{Q}_{upper} + \dot{Q}_{lower} - \dot{H}_s\left(\dot{M}_s\right) \tag{4}$$

Here, H_{film} is the electrode's enthalpy, $\dot{Q}_{upper}$ and $\dot{Q}_{lower}$ are the heat flux at the electrode's surface and bottom, and $\dot{H}_s$ is the enthalpy outflow due to solvent evaporation, which is dependent on the mass outflow $\dot{M}_s$. It is calculated using the mass transfer coefficient $\beta_{s,air}$, the molar mass M_s and molar density ρ_{air} of the surrounding air, the interface A_{inter}, and the gradient of the solvent's molar concentrations along the interface between the electrode film $y_{s,inter}$ and the surrounding air $y_{s,air}$. Furthermore, the Stefan correction factor K_{st} accounts for the influence of drag effects of evaporating molecules.

$$\dot{M}_L = \beta_{s,air} K_{st} M_s\, \rho_{air}(T) A_{inter}\left(y_{s,inter} - y_{s,air}\right) \tag{5}$$

The heat flow $\dot{Q}_{upper}$ is the product of the Ackermann correction factor K_A, the heat transfer coefficient α_{thermo}, the interface A and the temperature difference between dryer air T_{dryer} and electrode film T_{film}.

$$\dot{Q}_{upper} = K_A \alpha_{thermo} A_{inter}\left(T_{dryer} - T_{film}\right) \tag{6}$$

α_{thermo} is the sum comprising the radial and convective heat transfer coefficient. To estimate the heat transfer coefficients, a heat flux plate

was installed into the dryer in the location of one of the bottom air nozzles. Water flows through the plate, and the in- and outlet water temperatures are measured. With this temperature difference, the water's heat capacity and volume flow, the heat quantity is calculated. Using this heat quantity and the temperature difference between plate and dryer air, the heat transfer coefficients are determined. It is important to note that this measurement provides an estimation. Because the electrode's lower and upper part are both directly subjected to dryer air, the same heat transfer coefficient is assumed for the heat flow $\dot{Q}_{lower}$. Further details on the model is described in Kumberg et al. [38]

Table 4 shows the process parameters of the dryer and material properties of solvent and air, respectively. The heat transfer coefficients define the drying rate.

2.3.2. Binder-oriented simulation

The inhomogeneous distribution of binder occurring due to drying kinetics is modeled based on a cell model approach by Zihrul et al. [19] The authors are aware that some experimental publications suggest that the phenomenological idea behind this model does not consider individual mechanisms such as capillary transport, which is relevant to solvent and binder transport in an electrode during drying [38,41–43]. However, the application of this model was demonstrated, and it will be used to efficiently simulate binder migration in this study. The following transport equation is solved for every cell at each time step of the drying simulation:

$$\frac{\partial u}{\partial t} = D_{binder,solvent}\frac{\partial^2 u}{\partial x^2} - uv \tag{7}$$

The electrode wet film is divided into N equally sized cells along its layer thickness. At each time step, every cell k has a binder concentration $u_t(k)$ at time t. $D_{binder,solvent}$ is the diffusion coefficient of the binder in the solvent and v represents the film shrinkage rate. A detailed explanation of the binder-oriented simulation is found in Zihrul et al. [19], however, the following explains the most important steps:

Mass transfer due to diffusion takes place at every time step dt. The binder concentration $u_t(k)$ is calculated according to the following equations:

$$u_t(k) = u_{t-1}(k) + R_t\,(u_{t-1}(k+1) - 2u_{t-1}(k) + u_{t-1}(k-1)) \tag{8}$$

Here, $u_{t-1}(k)$ represents the binder concentration of the previous time step and R_t represents the dimensionless diffusion coefficient. The binder concentration for the first segment, meaning the segment in direct contact to the current collector is calculated as follows:

$$u_t(1) = u_{t-1}(1) + R_t\,(u_{t-1}(2) - u_{t-1}(1)) \tag{9}$$

The binder concentration of the last wet segment, k = N results from:

$$u(N_t) = u_{t-1}(N_t) + R_t\,(u_{t-1}(N_t - 1) - u_{t-1}(N_t)) \tag{10}$$

R_t is calculated as described in Eq. (11) and uses the effective diffusive coefficient $D_{eff}(t)$, the time step Δt and the segment size Δx for its computation. $D_{eff}(t)$ results from the current porosity of the wet film ε(t), the tortuosity of the electrode τ(ε(t)) and the diffusion coefficient $D_{binder,solvent}(t)$, all of which are constant over the electrode thickness.

$$R_t = D_{eff}(t)\frac{\Delta t}{\Delta x \Delta x} \tag{11}$$

$$D_{eff}(t) = \frac{\epsilon(t)}{\tau(t)}D(t) \tag{12}$$

The electrode tortuosity is estimated using the Bruggeman approach, see Eq. (13) and the diffusion coefficient is calculated with the Stokes-Einstein equation, Eq. (14).

$$\tau(t) = \epsilon(t)^{1-\alpha_c} \tag{13}$$

$$D_{binder,solvent}(t) = \frac{k_b T(t)}{6\pi\eta(t) r} \tag{14}$$

Hereby, k_b is the Boltzmann constant and η(t) is the current dynamic viscosity, which is interpolated according to [44]. T(t) is the current temperature and r is the hydrodynamic radius of the binder particles.

During the drying process, the virtual fluid level drops and passes the lower boundary of the cells. These cells are then considered "dry" and the binder they contained is transferred to the cell below. When the final film thickness is reached, the virtual fluid level stops moving, and binder transfer by diffusion continues. During this second phase, binder is continuously immobilized, and the increasing fraction of immobilized binder is not considered for transport by diffusion. It is assumed that the fraction of immobilized binder is equal to the fraction of dried pore volume. This is calculated based on the final electrode porosity and the remaining solvent volume.

2.3.3. Microstructure-oriented simulation

In order to model the microstructure formation during drying, the approach of Lippke et al. was adapted to anodes. The following paragraph briefly presents the model and discusses these adaptations.

In the first step, the simulation domain with a base area of 200 × 200 μm^2 and the height of the wet film thickness h_{wet} is created. h_{wet} is calculated based on the slurry recipe and the areal loading, as shown in Eq. (15). AL_{dry} describes the areal loading of the dried electrode. The mass fractions of the fluid and the solids are represented by x_f and x_s, while the densities of fluid and solid are described by ρ_s and ρ_f.

$$h_{wet} = \frac{AL_{dry}}{x_s}\left(\frac{x_f}{\rho_f} + \frac{x_s}{\rho_s}\right) \tag{15}$$

Particle shapes and a discrete particle-size distribution for the graphite active material are defined as described in Section 2.2. Since there was no filling algorithm that was able to distribute the needed number of particles in the simulation domain, the AM particles were inserted and shrunk to 10 % of their desired volume. Subsequently, they were grown up to their targeted particle size. Afterwards, a small repulsive force combined with a damping frictional stokes force was applied to the particles to randomly distribute them along the wet film volume. This described workflow is visualized in Fig. 3. Carbon black particles are represented as 1.5-μm-large, porous substitute particles, which represent carbon black agglomerates.

Bockholt and Mayer [31] have shown that carbon black can have an inner porosity between 30 and 80 % depending on the intensity of the preceding dispersion and dry-mixing process, thus the carbon black particles are also assumed to be porous. This is realized by increasing the number of 1.5 μm replacement particles and reducing their density accordingly.

As described for simulations of cathode-drying by Lippke et al. [32], the present simulations concerning anodes use surrogate models to represent fluid effects like evaporation. The system's viscosity is based on the solvent's viscosity and is increased due to the binder. Van-der-Waals (VDW) forces lead to carbon black structures that also increase

Table 4
Model parameter for anode drying simulations.

Dryer	Value	Unit	Source
Number of zones × length	3 × 2	m	Own measurement
Heat transfer coefficient zone 1	32	W m^{-2} K^{-1}	Own measurement
Heat transfer coefficient zone 2	32	W m^{-2} K^{-1}	Own measurement
Heat transfer coefficient zone 3	38	W m^{-2} K^{-1}	Own measurement
Material properties water 30 °C			
Heat capacity gas[a]	33.68	J mol^{-1} K^{-1}	[40]
Heat capacity liquid[a]	75.34	J mol^{-1} K^{-1}	[40]
Molar mass	0,018	kg mol^{-1}	
Vapor pressure[a]	4250	Pa	[40]
Evaporation heat[a]	43,756	J mol^{-1}	[40]

[a] Quantities are implemented as a function of temperature.

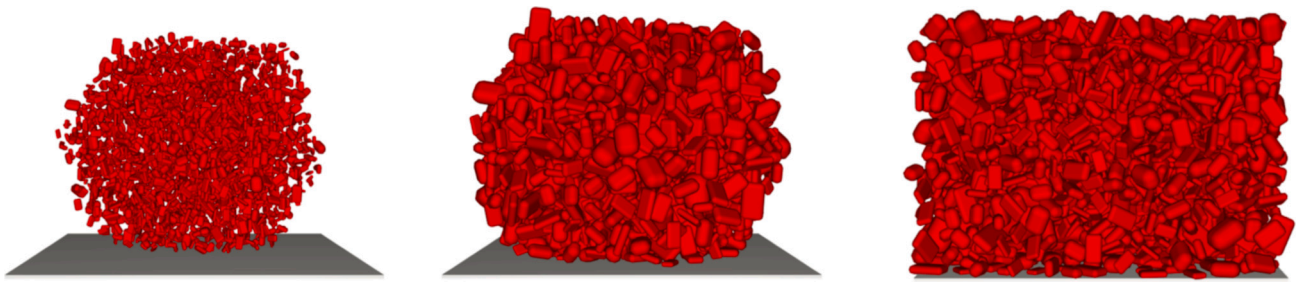

Fig. 3. Workflow for creating the initial particle arrangement for the anode drying simulation. Left: creating the particles with 10 % of their target volume, middle: gradually increasing the particles to their target size, right: evenly distributing the particles in the simulation domain.

viscosity, while steric interactions reduce the viscosity. It is therefore difficult to determine the exact viscosity of the slurry for the drying simulation, as it is dependent on temperature and solvent content, which is expected to change spatially in the course of drying. The measurements of Park et al. [45] and Reynolds et al. [46] suggest that SBR does not attach to the surface of the graphite particles, whereas CMC does. So, the viscosity of the fluid was assumed to equal the viscosity of an SBR-water solution which is a strong simplification. To depict the effect of the attachment of CMC to the graphite particles' surface, steric repulsion between all particles was implement based on the equations proposed by Ma et al. [47] Fig. 4 (a) shows the mechanical interaction forces between the particles within the drying simulation. These are attractive Van-der-Waals forces and repulsive steric forces, which both act between neighboring particles.

During drying, the virtual fluid level, implemented after Breinlinger et al. [48], is decreased at constant speed. Because no significant AM plastic deformation is expected during drying, the computationally most efficient, namely the Hertz model is used for contact force calculation. While lowering the fluid level, AM and CB particles are carried along. The microstructure is assumed to remain unchanged after the final film

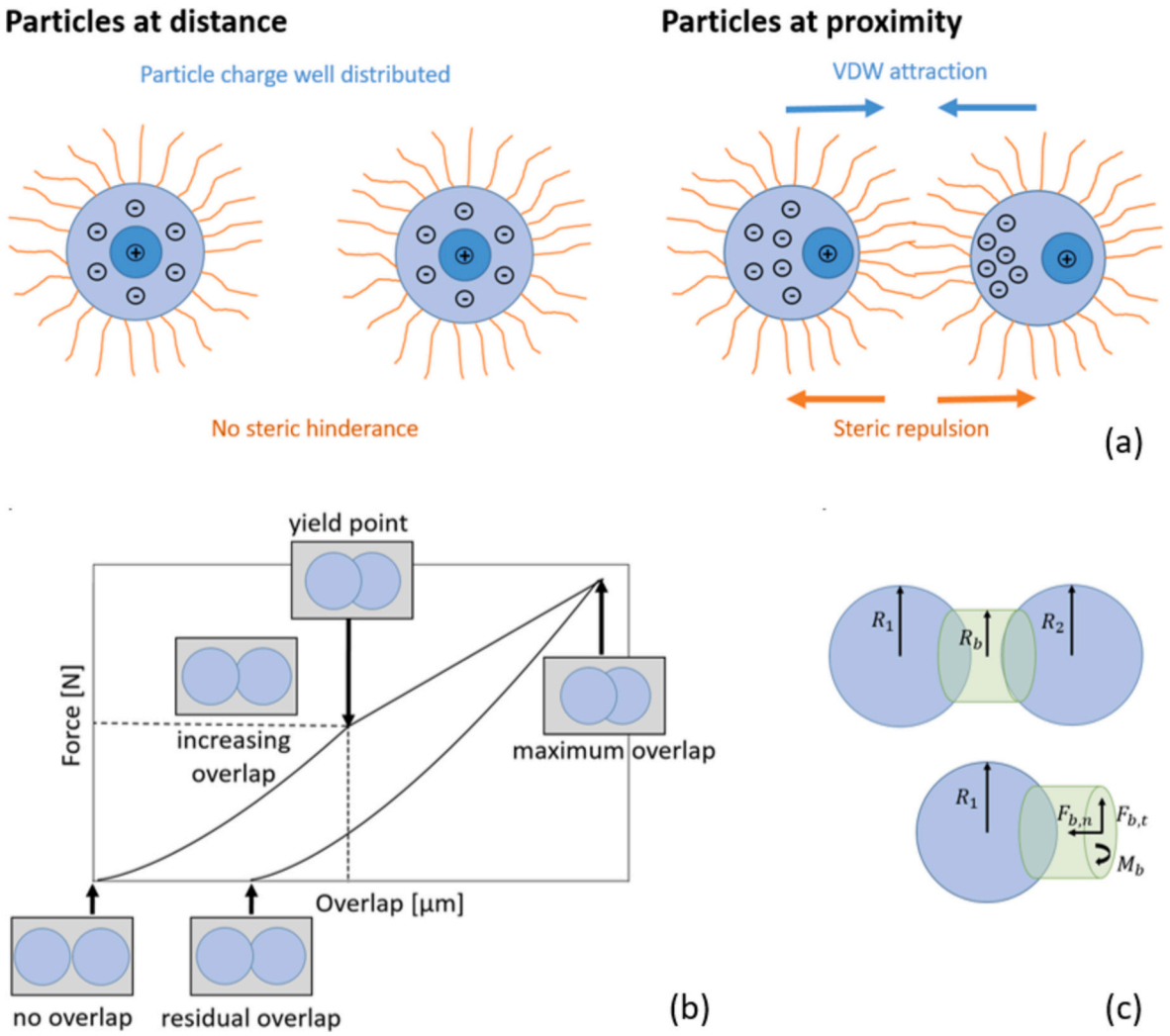

Fig. 4. Mechanical interaction forces between the simulated particles. (a) Van-der-Waals forces as attractive and steric forces as repulsive forces of neighboring particles in the drying simulation, (b) schematic of the Thornton-Ning model showing residual overlap as plastic deformation in the calendering simulation, after [24], (c) schematic of the bond model for the calendering simulation, after [24].

thickness has been reached. The CB distribution is assessed using the final DEM structure. Therefore the electrode is cut into 0.1-µm-large slices, with which the volumetric concentration of CB is calculated, and corrected considering the CB porosity.

Because of unrealistically high simulation times, scaling of forces was implemented to reduce computational cost. Hereby, the ratio of the particle's sinking velocity to the fluid level sinking velocity is kept constant. To decrease to simulation time by a factor k, other transient phenomena occurring in the simulation must be increased by the factor k. Details for this procedure are described in Lippke et al. [32] Finally, the simulation time was reduced by a factor of 10^5, which leads to losses in physical correctness, but allows for feasible simulation time. Drawbacks of the here conducted DEM drying model is, that the fluid menisci cannot be resolved. Furthermore, as no fluid dynamics are involved, the drying model cannot account for fluid currents and swarm effects during sedimentation. Having more knowledge about them would make the simulation more accurate, but would result in disproportionally higher computational cost.

2.4. Calendering simulation

In order to simulate the calendering process, a particulate microstructure, resulting from the prior drying simulations, is placed between two virtual plates as suggested by Sangros et al. [25] The lower plate represents the copper current collector, while the upper plate represents the calender roll. A translational motion is attributed to this "calender-roll" plate, so that the plate moves down on the particle bed, compresses it to the required normal stress and moves up again. As observed in actual calendering processes, the particle bed is compressed to a certain thickness and relaxes back several micrometers after the compression, depending on the experienced compression depth and electrode formulation. Fig. 5 shows the starting point of every calendering simulation, the midpoint, where the top plate compresses the particle bed to the minimum thickness, and the end state, after which the plate has moved up again and the microstructure has relaxed. The elastic and plastic deformations involved in the process of compaction are modeled within this virtual set-up.

In order to determine whether the particle shape had an influence on resulting stresses and final film thicknesses for calendering, three different particle sets were compared in individual calendering simulations. The first set consisted of spherical particles, the second one is the set named "use case", described in Section 4.1 and the third adopted an even flatter shape for all particles, named "flat". Table A2 lists their vertical and horizontal aspect ratios, as well as their number of corners. Fig. 1 visualizes their geometries. All particle templates within one particle set adopted the particle size distribution listed in Table A1.

Various contact models like the Hertz model, the EEPA or the Thornton-Ning model have been used to describe the mechanical behavior between particles during the calendering process [13,25,49]. In our preliminary studies, the Thornton-Ning model [26] showed the best ability to describe the model anodes, as it offers the ability to depict not only elastic, but also plastic deformation. The Thornton-Ning model and the corresponding qualitative particle overlap is schematically displayed in Fig. 4 (b). Furthermore, solid-state-bridges (bonds) have been deployed to display the inactive material as suggested by Sangros [25]. They are qualitatively visualized in Fig. 4 (c). Bonds were created at the beginning of the simulations, whenever the distance between two particles was smaller than a certain distance criterion, see Eq. (16). The calculation of this threshold was adapted to the herein used non-spherical particle shapes. The parameter c is a control parameter, while r_i and r_j each represent half of the two involved particle's sizes. The bond radius is calculated by multiplying half of the size of the smaller particle by another calibration parameter, denoted as α, see Eq. (17). Because the binder migrates during the drying process [50,51], the electrode was divided into three equally-sized segments along the electrode height, as suggested by Sangros et al. [52] The value for α was adjusted for each segment, so that the binder gradient was represented by a gradient in the bond volume.

$$d_{i,j} < (r_i + r_j) + (r_i + r_j) \cdot c \tag{16}$$

$$r_b = \alpha \bullet min(r_i, r_j) \tag{17}$$

Bonds were also created between particles and current collector.

$$r_b = \alpha \cdot r_i \tag{18}$$

α is set so that the volume proportion of the cylindrical bonds corresponded to the volume proportion of the inactive material, i.e. carbon black and binder, in the electrode.

While particles can only transmit forces, bonds can transmit forces and moments in normal and tangential direction. As described by Sangros et al. [24], the incremental forces $F_{b,n}$ and $F_{b,t}$ and moments $M_{b,n}$ and $M_{b,t}$, both in normal and tangential direction, are calculated for each time step dt, based on the bond's normal and tangential stiffness S_n and S_t. J denotes the polar moment of inertia.

$$dF_{b,n} = -v_n \cdot S_n \cdot A \cdot dt \tag{19}$$

$$dF_b, t = -v_t \cdot S_t \cdot A \cdot dt \tag{20}$$

$$dM_{b,n} = -w_n \cdot S_n \cdot \frac{J}{2} \cdot dt \tag{21}$$

$$dM_{b,t} = -w_t \cdot S_t \cdot J \cdot dt \tag{22}$$

In normal and tangential direction respectively, v_n and v_t are the relative velocities between bonded particles and w_n and w_t are the relative angular velocities.

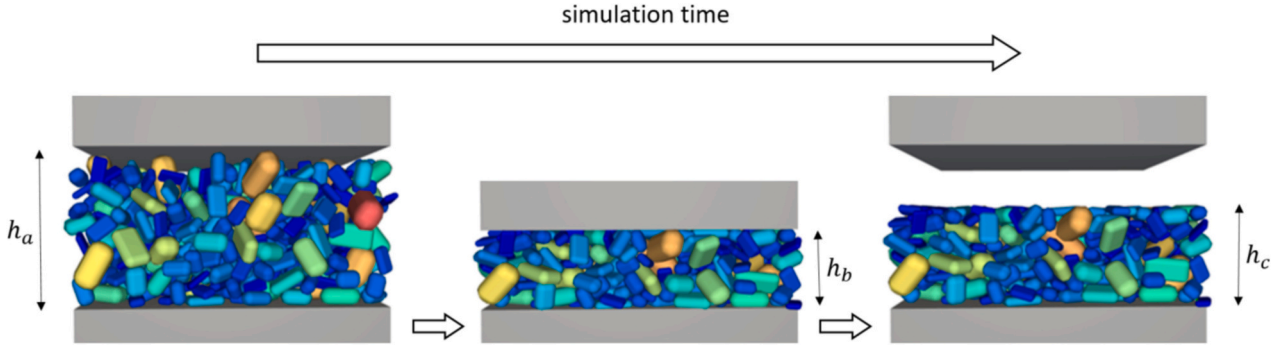

Fig. 5. Visualization of the simulated calendering process. h_a is the initial thickness of the coating, h_b denotes the coating thickness at minimum roll gap, which is equivalent to the roll gap itself and h_c is the final coating thickness after the electrode relaxes from the pressure applied by the roll.

3. Coupling of drying and calendering

The three drying models presented have different objectives. The drying-kinetics simulation plays a key role, as it provides input parameters for the binder and microstructure simulation. The microstructure simulation calculates the film shrinkage rate based on the drying rates of the drying-kinetics simulation. The film thicknesses and porosities determined in this way are transferred to the binder simulation. In addition to the structural information, the binder simulation uses the drying rates of the drying-kinetics simulation as well as the film temperature. While the drying rate is considered to describe the sinking of the film and the remaining solvent content, information about the film temperature is used to determine the solvent viscosities and the diffusion coefficients during the simulation.

As described in Section 1, the inactive material distribution in the calendering model by Sangros et al. [24] is represented by the local volume of the solid bridges. The particle structure at the end of the microstructure-oriented drying simulation is used as the input parameter for the calendering simulation. To avoid a double representation of the inactive material, only the AM particles are transferred to the calendering simulation. The local CBD distribution derived from the drying simulations are combined. The inactive material distribution is averaged within three equally sized segments along the electrode height, analogous to Sangros et al. [52] These average volume concentrations are used as the target value for generating the bonds in the respective segments. The previously presented control parameter c is selected so that each active material particle is connected to the bond network to ensure a realistic and numerically stable electrode structure. The parameter α is then selected within each segment so that the volume of the bonds corresponds to the target volume concentration. This is followed by the calibration of the mechanical bond parameters stiffness and damping. These parameters are assumed to be constant for all areal loadings and for all sections of the electrode. Locally varying compositions of the inactive material are not taken into account in order to keep the calibration effort manageable.

4. Results and discussion

4.1. Drying kinetics simulation

The here employed model depicts the film temperature and the solvent loading over the course of the drying process. The drying rate is calculated from the change in solvent loading over time. Fig. 6 shows the results of the model. As there is no change in the drying temperature or the flow conditions between the first two dryer segments, there is no change in the drying rate and the film temperature. Later in the drying process, the film temperature begins to rise due to the final film thickness being reached, which is defined to be the case when the liquid surface sinks below the coating film surface. This results in a slightly lower evaporation rate due to transport limitations within the electrode structure. At higher areal loadings, more time is required to reach the final layer thickness, which is why the increase in film temperature occurs later. The model electrodes with the two highest areal loadings are not yet completely dried before arriving in the third dryer segment, in which the flow of dryer air to the electrode changes from indirect to direct. Consequently, an additional increase in the film temperature is observed from this point onwards.

The drying rates and film temperatures in the respective dryer segments were averaged for the transfer to the structure-oriented and binder-oriented simulations (Table 5).

4.2. Microstructure-oriented simulation

Table A3 in the Appendix lists the modeling parameters of the drying simulation and Fig. 7 shows the results of the structure-oriented drying simulation that used the aspherical particles from particle set “use case”.

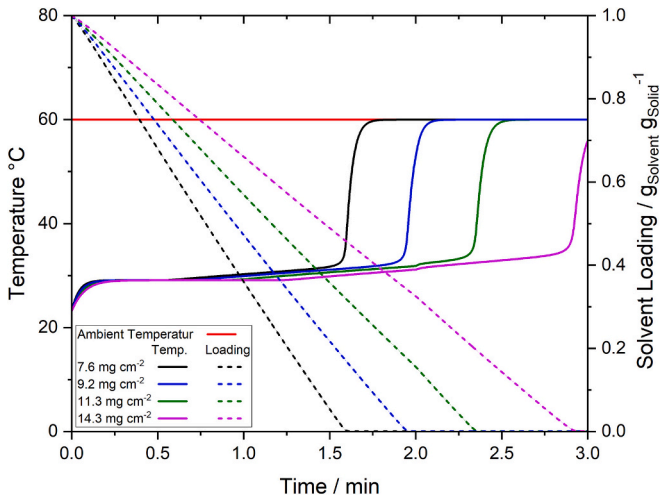

Fig. 6. Simulated drying kinetics for the areal loadings 7.6 mg cm^{-2}, 9.2 mg cm^{-2}, 11.3 mg cm^{-2} and 14.3 mg cm^{-2}.

The descent rate of the liquid film was set according to the drying kinetics simulation. By calibration, a value of 80 % was selected for the carbon black porosity, while the interparticulate friction coefficient is assumed to be 0.85. Overall, there is a very good fit between the experiment and the simulation in terms of layer thickness and the linear rise in porosity. This illustrates the suitability of the scaling approach used and the selected particle templates visible in Fig. 7. Fig. 7 also shows an exemplary particle structure before and after drying.

Fig. 8 shows the CB distribution along the layer thickness of the simulated final structures. A clear peak in the carbon black concentration is visible near the electrode surface, which is due to the sinking liquid front. Except for the area close to the current collector, a constant carbon black concentration can be seen in all areas of the electrode. A reduced carbon black concentration is observed directly above the current collector, as the flake-shaped graphite particles are concentrated at the current collector by sedimentation and thus block the area for carbon black particles.

For the experimental investigation of the spatial carbon black distribution for an anode, Weber et al. observed a carbon black accumulation via spectrophotometry at the electrode surface due to drying effects [53]. Pfaffmann et al.[51]investigated the carbon black distribution on model anodes dried at different speeds using energy-selective backscattering detection during scanning electron microscopy and an evaluation algorithm developed in-house. Similar to the simulation presented here, they observed a relatively constant carbon black concentration in the lower third of the electrode and a strong increase towards the electrode surface. In Pfaffmann’s measurements, the area of increased carbon black concentration in the upper electrode segment is significantly larger relative to the electrode thickness. However, a

Table 5
Drying rates and film temperatures in the three drying zones of all areal loadings. Drying rates in parenthesis are used within the binder-orientated model, but not in the structure-orientated model, since the binder migration is still ongoing after the final electrode thickness is reached.

Electrode	Zone 1 [g s^{-1} m^{-2}]	Zone 2 [g s^{-1} m^{-2}]	Zone 3 [g s^{-1} m^{-2}]
7.6 mg cm^{-2}	0.81	(0.77)	–
9.2 mg cm^{-2}	0.81	(0.77)	–
11.3 mg cm^{-2}	0.81	(0.78)	(0.85)
14.3 mg cm^{-2}	0.81	0.80	(0.85)
	Zone 1 [°C]	**Zone 2 [°C]**	**Zone 3 [°C]**
7.6 mg cm^{-2}	29.41	31.05	–
9.2 mg cm^{-2}	29.24	31.04	–
11.3 mg cm^{-2}	29.1	30.59	32.77
14.3 mg cm^{-2}	29.06	29.9	35.85

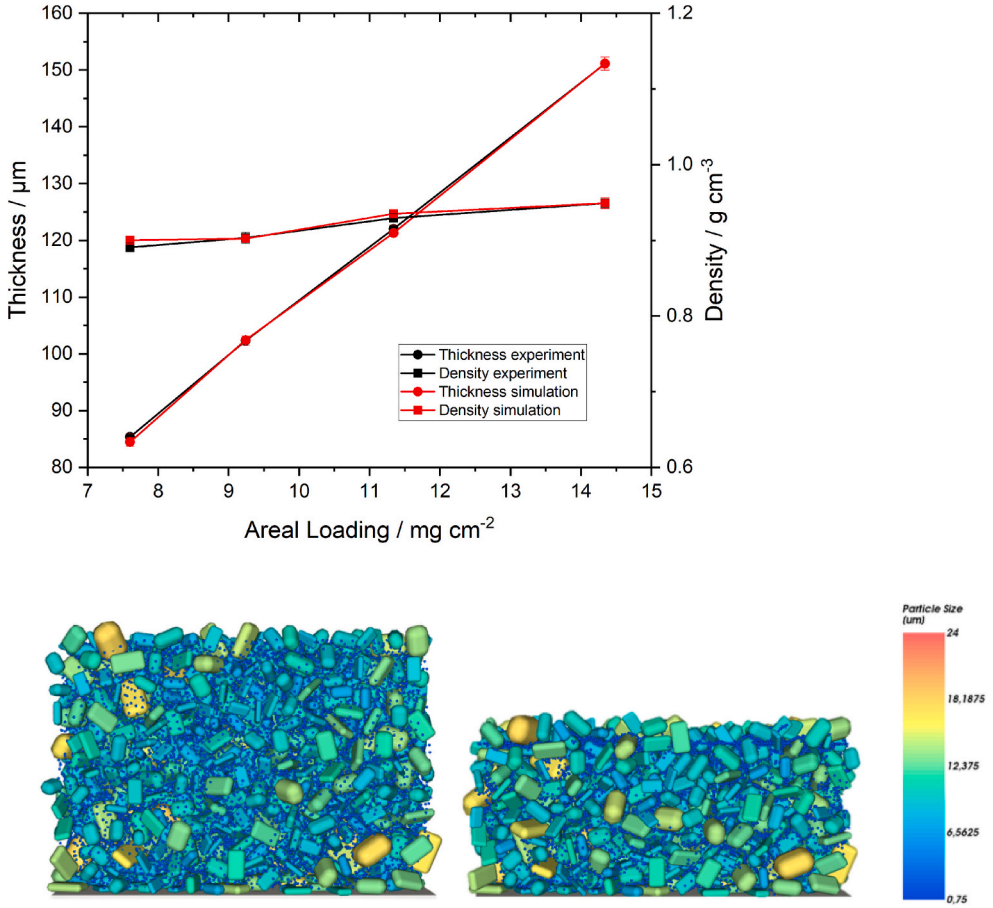

Fig. 7. top) Film thickness and film density over the areal loadings after the drying simulations, bottom) visualization of the anode structure before and after drying.

comparison proves to be difficult, as the model electrodes used by Pfaffmann had a thickness of 400 µm. These results are also consistent with the observations of Luo et al. [41], who observed that when drying a suspension of latex and ceramic particles, the smaller ceramic particles are pushed into the cavities between the larger latex particles.

Due to numerical instabilities, it was not possible to reconcile diffusive effects with the force scaling approach. It can therefore be assumed that the carbon black concentration at the electrode surface is overestimated. In addition, it is possible that the greatly increased diameter of the carbon black particles due to coarse graining also distorts their distribution. However, this error has no effect on the transfer to the calendering simulation, as an error here would not change the local mean value of the carbon black concentration per electrode third, which is the value used for further simulations.

4.3. Binder-oriented simulation

The binder segregation modeled according to Zihrul et al. [19] and the estimated film temperatures and drying rates modeled according to Kumberg et al. [38] were used to calculate the solvent loading along the dryer.

Fig. 9 visualizes the binder distribution in the dried anodes for all four areal loadings. In agreement with previous cathode drying simulations [10,54] and other publications [51,55], binder segregation takes place in all areal loadings, but most prominently at the highest loading.

A value of 3 was selected for the Bruggemann coefficient to represent the flake form of the graphite [56]. For simplification, it was supposed that SBR and CMC behave identically so that both binder species could be considered together. In addition, it was assumed that no binder adhered to the particles because the binder content adhering to the particles could not be determined. The hydrodynamic radius of the binder was assumed to be 5 nm [57,58]. No experimental validation of the results was carried out, as the possibility of labeling the SBR using osmium was not available and the dissociation of the Na-CMC discredits the quantitative significance of the mapping of sodium for mapping the CMC distribution.

Analogous to similar simulations regarding cathodes [15], there is an increase in the binder volume fraction towards the electrode surface. The gradient becomes stronger with increasing areal loading. Thus, despite various simplifications and assumptions, the result of the modeling is consistent with experimental investigations.

4.4. Coupling of binder and carbon black

As described above, the carbon black, obtained by the DEM drying simulations (Section 4.2), and the volume fractions of the binder, obtained by the binder simulation (Section 4.3), are combined and used as target values for the bond volume concentration. Fig. 10 shows the determined inactive material volume fractions for the different areal loadings and regions within the model anodes. An increase in the inactive material gradient is observed with increasing areal loading, which is consistent with the literature [3,59]. Table 6 shows the values of the calibration parameter alpha α, which were used to compute the target values for the inactive material volume fraction [60].

5. Calendering

5.1. Influence of particle shape

First, the influence of the different particle shapes is assessed

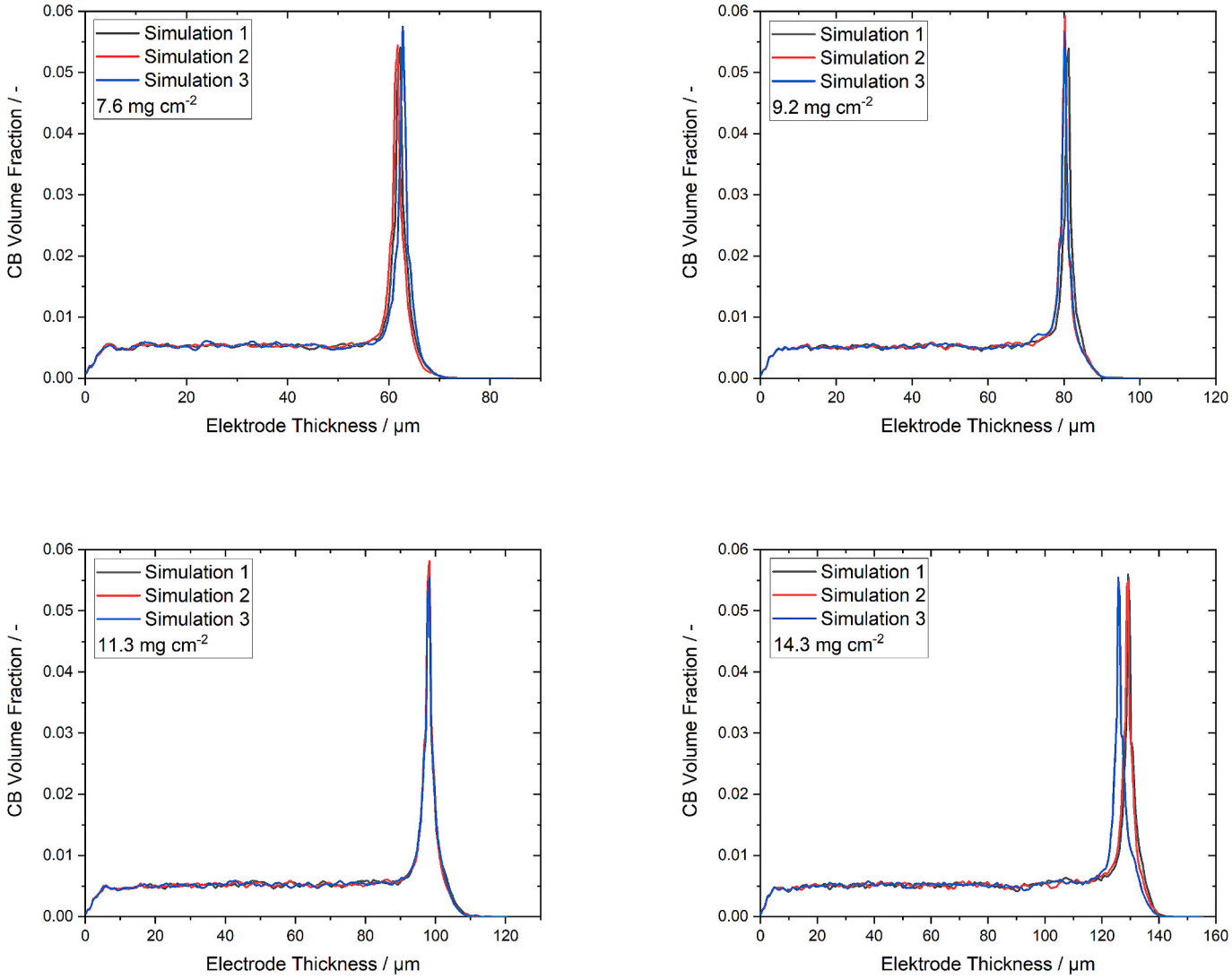

Fig. 8. Simulated distribution of CB along the film thickness for all four ALs.

qualitatively. For this purpose, the initial structures for calendering were created stochastically. Fig. 11 shows that the spherical particles lead to the highest stresses within the particle bed during calendering, and the flatter the particles, the lower the internal stresses. A clear trend for the final coating thickness is also observed: The flatter the particles, the lower the final thickness. Both trends are due to the ability of non-spherical particles to rearrange better, i.e. to lower porosities, in the particle bed. Before any plastic deformation of the particles, the particle bed consisting of spherical particles has reached its densest packing much earlier. This means that stresses due to the start of plastic deformation occur earlier, too.

Taking the dried electrode structure as an input, the calendering data for the areal loading of 11.3 mg cm^{-2} was used to calibrate the calendering model. Within the bond model, the dimensionless bond damping coefficient [25] is fitted to 0.9997 and the normal and tangential bond stiffness S_n and S_t each amount to $3.357 \bullet 10^{12}$ N m^{-3}. The dimensionless yield point [25] of the Thornton-Ning normal force model is fitted to 0.005. Since the mechanical behavior of graphite particles is governed by anisotropy and their irregular shape, the Young's modulus of the particles was treated as a calibration parameter and 1.476 GPa were calibrated as Young's modulus, which can be considered a reasonable value [61–64].

Fig. 12 shows the simulated calendering processes for the four ALs. In addition to this, Table A4 in the Appendix displays the numerical values for coating thickness at roll gap, stresses at roll gap and final coating thicknesses for experiments and simulations of all ALs. As previously mentioned, the simulated dried electrode structure of the particle templates displayed in Fig. 1 and the calculated inactive material distribution were used as input. The simulations were carried out stress-controlled, which means that the virtual electrodes were densified until the experimentally measured stress was reached. The simulation results fit the experimentally obtained values of AL 11.3 mg cm^{-2}, which was used for calibration, and AL 9.2 mg cm^{-2} very well for the first three calendering degrees, whereas the gap width of the highest loading are clearly underestimated. At the smallest AL the gap width is slightly overestimated by the simulation for the first three calendering degrees before it underestimates the stress. Except for the highest areal loading the simulation can predict the final thicknesses of the electrodes with reasonable accuracy for the first three calendering degrees. The mentioned deviations for higher calendering degrees and the highest areal loading can be explained by the high fraction of plastic deformation, which is discussed in the following section. The results show, that the chosen Thornton-Ning model is not able to depict such a high fraction of plastic deformation. In the Thornton-Ning model, the contact force during unloading is calculated using Hertz theory, and the plastic deformation is governed solely by the portion of the loading curve above the yield point. Upon unloading, the contact force calculations mirror the loading calculations. As shown in this study, this approach

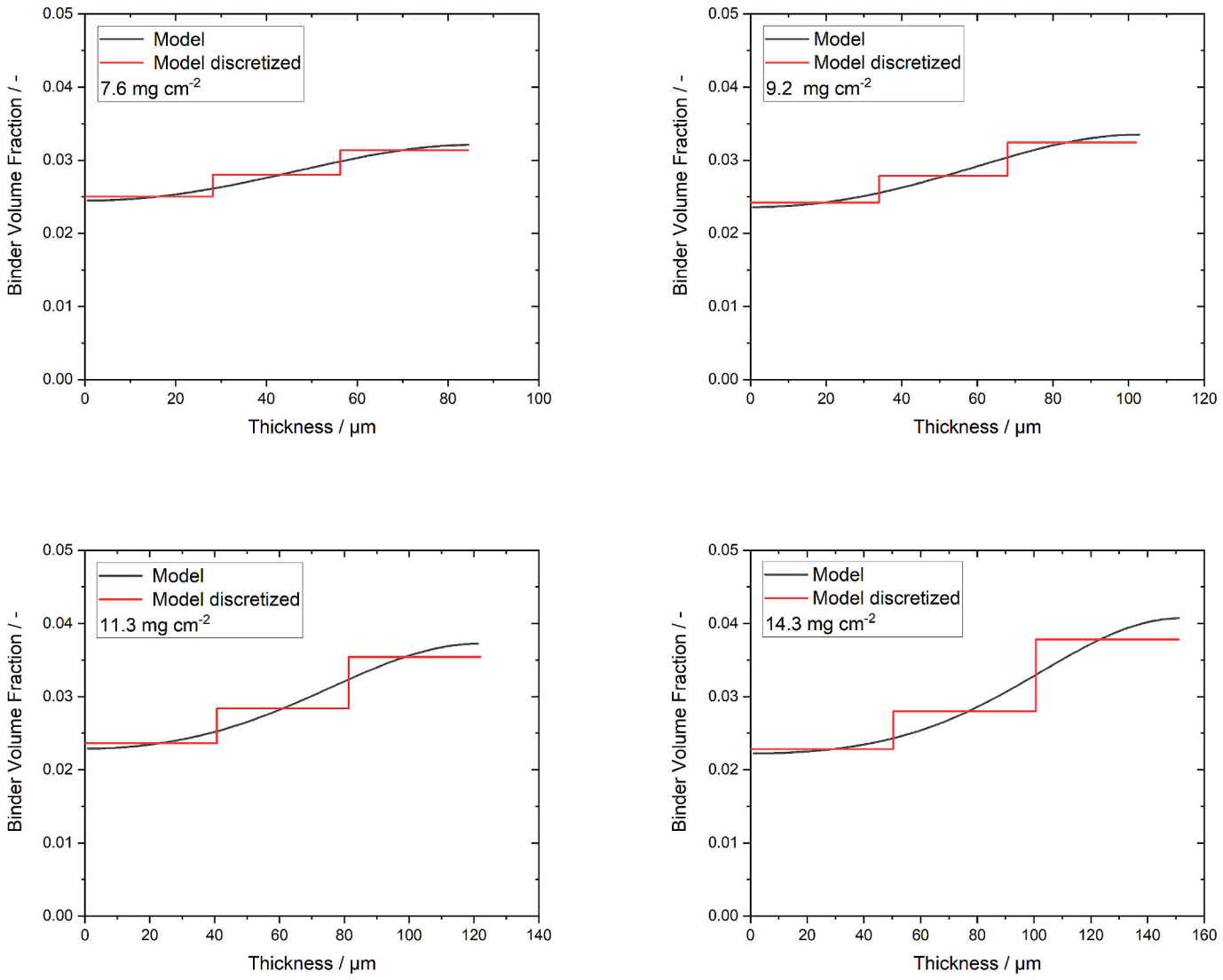

Fig. 9. Modeling results of binder distribution (gray) and discrete binder distribution after dividing the anode in three segments along the film thickness (red) for all four Als. (For interpretation of the references to colour in this figure legend, the reader is referred to the web version of this article.)

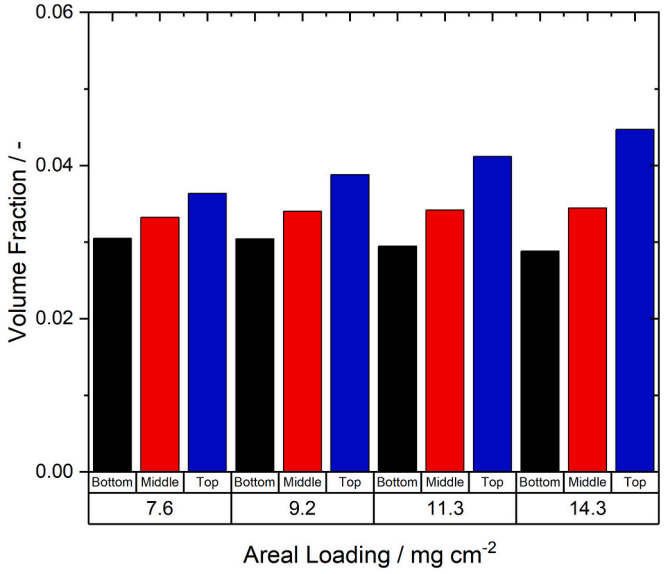

Fig. 10. Inactive volume fractions for the four areal loadings.

Table 6
Values for α for each section in each AL.

AL [mg cm^{-2}]	α_{bottom} [−]	α_{middle} [−]	α_{top} [−]	$L_{b,max}$ [µm]	c [−]
7.6	0.2994 ± 0.0009	0.3304 ± 0.0010	0.4539 ± 0.0062	3.5	4.0
9.2	0.3084 ± 0.0013	0.3407 ± 0.0079	0.4527 ± 0.0040	3.5	4.0
11.3	0.3068 ± 0.0024	0.3453 ± 0.0006	0.4489 ± 0.0031	3.5	4.0
14.3	0.3017 ± 0.0017	0.3431 ± 0.0012	0.4535 ± 0.0073	3.5	4.0

inadequately accounts for the plastic deformation of anodes during calendering. To address this, models that incorporate greater plastic deformation while maintaining the required force levels are needed. Alternatively, particle breakage models could be employed in future calendering simulations to better describe the significant plastic deformation of graphite particles.

To account for as much plastic deformation as possible within this model, at least for smaller calendering degrees, the yield parameter had to be chosen rather low, which explains the underestimation of the calendering stress for higher calendering degrees.

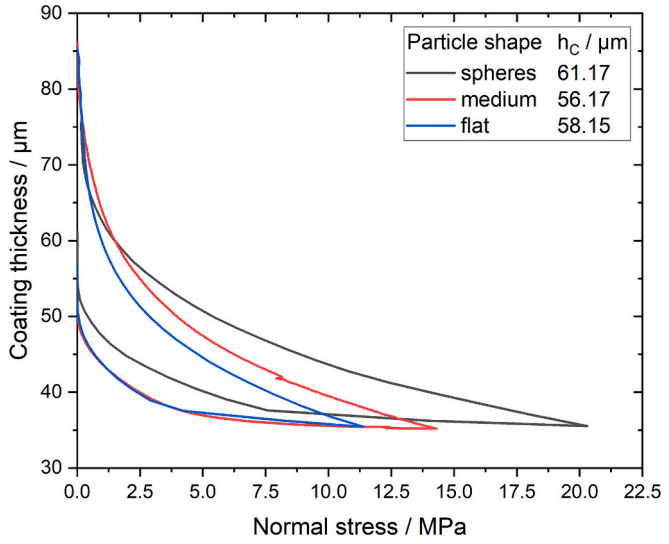

Fig. 11. Influence of particle shape on stress and final coating thickness during calendering.

Fig. 13 shows the experimentally and simulatively determined layer thicknesses after calendering as a function of the line load. Except for the highest areal loading already discussed, there is fair agreement for the final layer thickness by the chosen Thornton-Ning model. This information can be used as a decision support in the electrode production. If a production line desires to change the areal loading of the electrodes to be produced, existing calendering data can be used to calibrate the calendering model. With this a line load can be suggested to the calender operator to reach a desired electrode density. The deviation for the highest areal loading will be discussed in the following chapter. To set up the initial microstructure of the electrode, which will be virtually calendered, the drying approaches described earlier was used.

The findings shown in this study agree with previous calendering simulations concerning the need for plasticity in the used contact models [20,25,49,65]. Most studies focus on cathode calendering, which involves spherical particles in the simulations. Weitze et al. recently took into account the slight non-sphericities of NMC particles by resolving these particles via a highly sophisticated method using Micro-CT images. They and other research groups, however, demonstrated a smaller scope of validity, which limits the applicability of their calendering model [23,49]. Within the present study four areal loading were modeled using one contact model with one parameter set, showing large validity of the model. Furthermore, the topic of anode calendering was addressed, which includes the difficult representation of anisotropic, non-spherical graphite particles.

6. Experimental analysis

The experimentally calendered anodes are analyzed regarding their spring-back over stress, which is displayed in Fig. 14. The spring-back

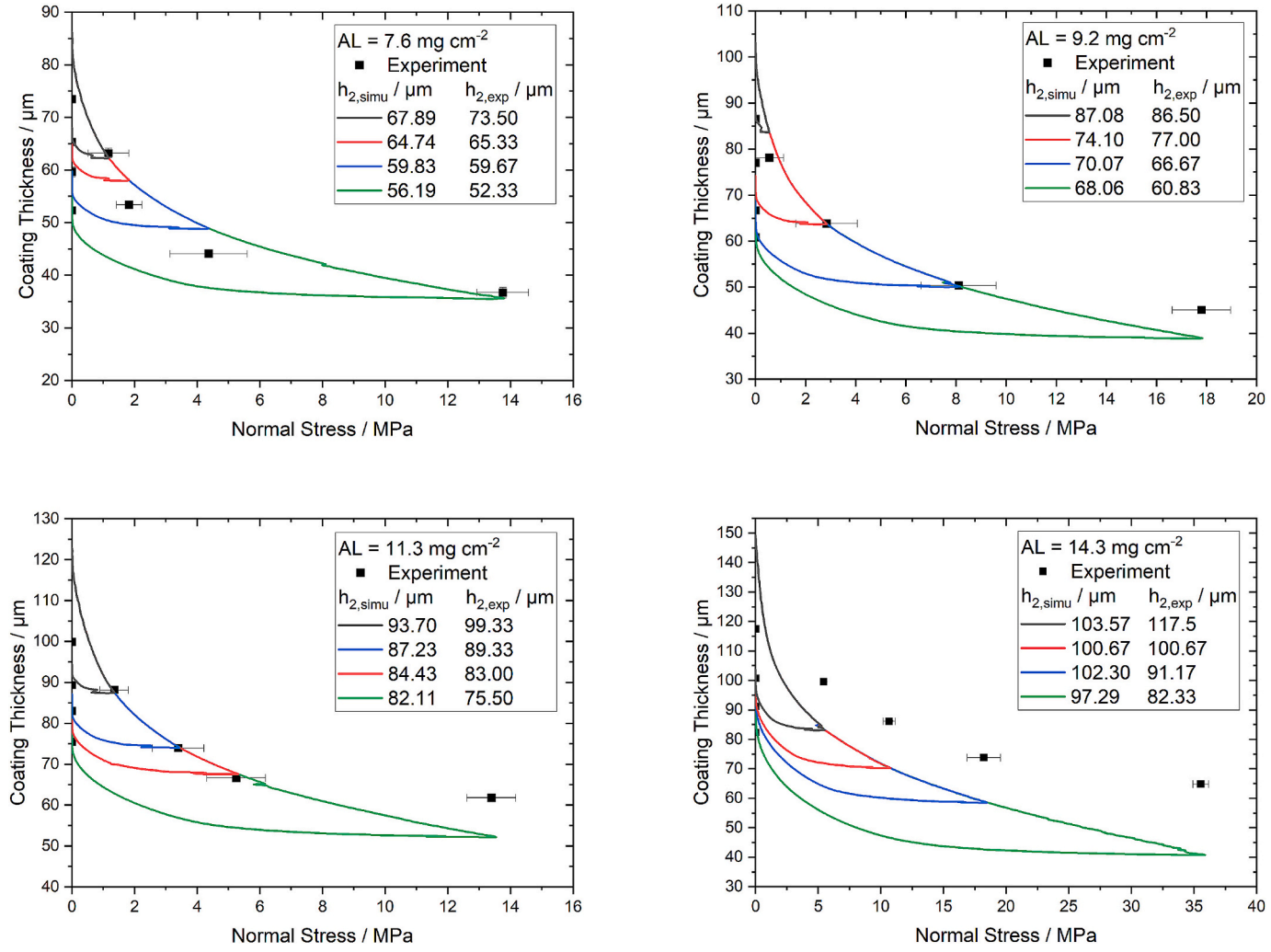

Fig. 12. Film thickness over stress obtained by calendering simulations for all areal loadings.

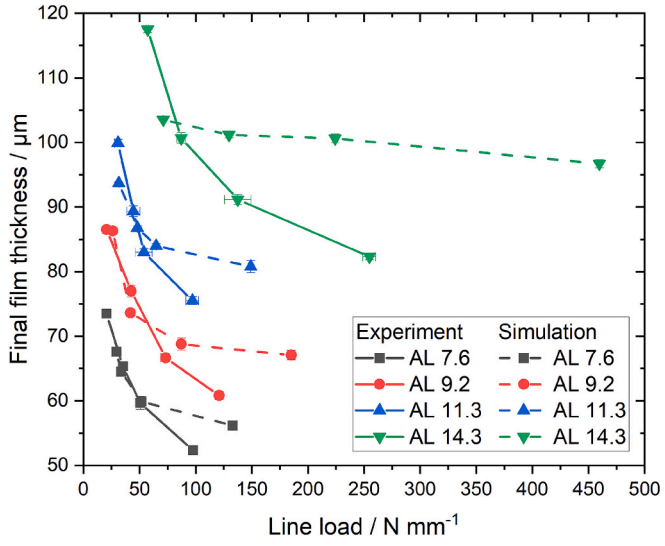

Fig. 13. Experimental and simulated final film thickness vs applied line load.

increases linearly until stresses of approximately 4 MPa are reached. After that, the spring-back stays constant over a wide range of stresses. The higher stresses do not lead to a further increase in elastic, but rather to a sole increase in plastic deformation. An explanation for the absence of further elastic deformation might be breakage of particles, which, for graphite particles would be the sliding of graphene layers against each other [62].

Nanoindentation confirms the almost constant elastic spring-back (SB) over a wide range of stresses, as the SB only slightly increases with increasing calendering degree. The elastic SB only increases by 1 µm when increasing the indenter load from 160 mN to 200 mN, corresponding to a 40 µm deeper indentation. This matches the previous findings of constant SB after a certain applied force. The transition stress was determined to be 5 MPa, which, taking under consideration the 50-µm indenter flat punch, corresponds to an indenter load of 9.82 mN. The depth corresponding to 9.82 mN of load is 3 µm. The nanoindentation measurements are performed well above this depth, so it goes along with the findings from calendering that the absolute elastic SB for all indentation depths of 20 µm, 40 µm, 50 µm and 60 µm are similar to each other. These observations are consistent with the results of Khelifa et al. [66], who also observed almost complete plastic deformation beyond a yield point at 1.9 MPa during the nanoindentation of graphite layers. In contrast to the results obtained from the here studied anodes, cathode calendering shows an increasing springback at higher line loads [30]. This results in a better fit of common DEM contact models when simulating the calendering process of cathodes [15].

In addition, cross-sections of differently calendered anodes were examined using scanning electron microscopy to optically record the plastic deformation of the graphite particles. Fig. 15 compares a cross-sectional image of an uncalendered anode with that of a heavily calendered anode (1.71 g cm^{-3}). Due to the irregular particle shape, it is not possible to detect plastic deformation when looking at individual particles. However, the extent of the plastic deformation becomes clear when looking at the particle shape and arrangement in comparison to the uncalendered electrode: The highly calendered anode shows a low-porosity arrangement, which cannot be achieved by mere rearrangement, but only by strong plastic deformation.

By evaluating the absolute elastic recovery during calendering, nanoindentation measurements on electrodes and SEM images of electrode cross-sections, the hypothesis was confirmed that a strong plastic deformation of the graphite particles takes place during the calendering of anodes,

Thus, the strong deviation in the model's recovery at higher calendering degrees and the highest basis weight appears to be a consequence of reaching the yield stress of individual graphite particles at least locally, even at low degrees of compaction. The used Thornton-Ning model is capable of mapping plastic deformation of particles, but not to the extent observed. In the future, a contact model would have to be developed that completely reproduces plastic deformation from a defined point onwards. For example, the relief curve of the Thornton-Ning model could be adapted for this purpose. Instead of the previous relief according to Hertz, a steeper stress drop could be computed, which would result in a higher plastic deformation. This relief could be implemented as a function of the maximum stress reached, so that the partial elastic recovery for low compression and the complete plastic deformation for higher compression are mapped. A calibration using nanoindenter measurements as in Fig. 14 would be conceivable.

7. Conclusion

In this study, three models representing different aspects of drying were successfully combined to describe the kinetics, structure formation and binder segregation during anode drying. The aspherical shape of graphite particles was taken into account by using a non-spherical set of particles for the DEM simulation. The layer thickness and porosity could be validated with experiments, and the binder model delivered plausible results. This information was successfully transferred to a calendering simulation. First, the influence of the particle shape on the calendering process was investigated on stochastically created particle structures. It was found that a higher degree of sphericity leads to higher calendering stress and a more pronounced spring-back effect. Using model anodes, it was demonstrated that the calendering setup can reproduce the mechanical behavior of anodes during calendering for moderate densification. The deviations at higher calendering stresses could be attributed

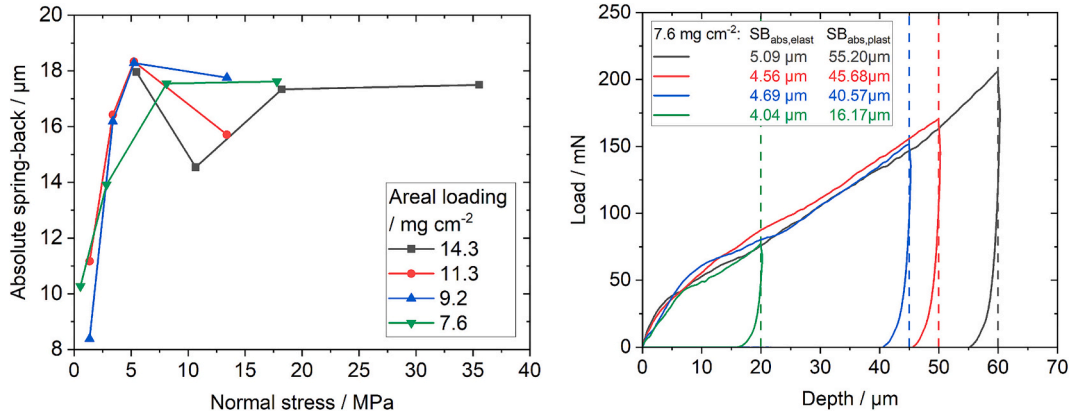

Fig. 14. Absolute spring-back over stress obtained by calendering (left); nanoindentation results showing plastic and elastic deformation (right).

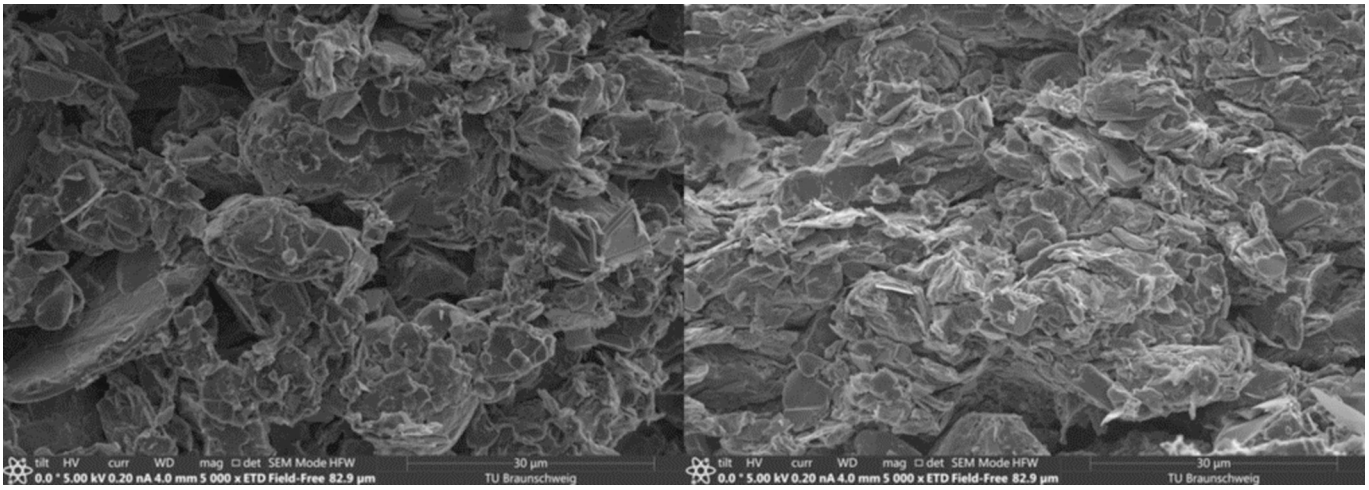

Fig. 15. SEM cross-sectional images of an uncalendered (left, 0.93 g cm^{-3}) and heavily calendered (right, 1.71 g cm^{-3}) anode. Areal loading = 11.3 mg cm^{-2}.

to the fact that anodes beyond a certain calendering stress only exhibit an increase in plastic deformation behavior. Beyond stresses of 5 MPa, the elastic deformation behavior stays constant. This explains why the calendering of higher areal loadings, which requires more force for compaction, cannot be captured by the simulation. This observation was additionally confirmed by nanoindenter measurements and is consistent with nanoindentation measurements on flexible graphite layers from the literature.

In future work, the binder segregation of the anodes should be determined experimentally to validate the binder model. In addition, a methodology should be developed that generates model graphite particles by means of image evaluation. Machine learning approaches, for example, would be conceivable. Images of single graphite particles could be processed by machine learning algorithms that convert these 2D images into 3D particle models, which could then be imported into the drying and calendering simulations. A methodology to do so could be the one described in Giannis, Thon et al [67], which will also be incorporated in our future research. Other useful machine learning applications could involve identifying grain sizes and distinguishing between different materials from anode cross section images. This application would support the validation of the resulting simulated microstructures. Finally, a contact model should be developed that is able to model high levels of plastic deformation better than the Thornton-Ning model.

CRediT authorship contribution statement

Mark Lippke: Writing – review & editing, Writing – original draft, Visualization, Validation, Supervision, Project administration, Methodology, Investigation, Formal analysis, Data curation, Conceptualization. **Caroline Willuhn:** Writing – review & editing, Writing – original draft, Visualization, Validation, Methodology, Investigation, Formal analysis, Data curation, Conceptualization. **Tobias Ohnimus:** Writing – original draft, Methodology, Formal analysis, Data curation. **Thilo Heckmann:** Writing – original draft, Methodology, Investigation. **Philip Scharfer:** Writing – original draft, Project administration, Methodology. **Wilhelm Schabel:** Resources, Project administration, Funding acquisition, Conceptualization. **Carsten Schilde:** Project administration, Funding acquisition, Conceptualization. **Arno Kwade:** Supervision, Resources, Project administration, Funding acquisition, Conceptualization.

Declaration of competing interest

The authors declare that they have no known competing financial interests or personal relationships that could have appeared to influence the work reported in this paper.

Acknowledgements

The authors gratefully acknowledge the financial support by the Federal Ministry for Education and Research (BMBF) within the research project “Sim4Pro” (03XP0242A). Furthermore, we would like to thank Alexander Diener and Finn Frankenberg for several discussions and Michael Bredekamp, Stoyan Ivanov, Alexander Neuberger and Stephanie Michel for their help with the experiments. In addition, the authors would like to thank Lucas Kostetzer for his valuable advice. Mark Lippke and Caroline Willuhn contributed equally to this publication.

Appendix

Table A1
Particle size distribution of the particles employed in all simulations.

L / µm	Cumulative / %
23.3	100
19.0	80.1
16.3	60.2
14.9	40.0
12.1	20.0

Table A2
Geometrical parameters for the particles template "flat".

Template: flat	1	2	3	4	5
Vertical aspect ratio	1.65	1.85	1.95	1.65	2.3
Horizontal aspect ratio	0.65	0.45	0.35	0.75	0.75
Corners	6	6	6	6	6

Table A3
Modeling parameters of drying simulation.

Parameter	Value	Source
Young's modulus graphite	1.476 GPa	Calibration based on preliminary studies in the range of [61,68–70]
Density graphite	2.26 g cm^{-3}	[7]
Young's Modulus carbon black	5 GPa	[61,68,70]
Density carbon black (assumption: Pores filled with water)	1.132 g cm^{-3}	[7]
Viscosity binder solution	0.045 Pas	[46]
Density water	1.003 g cm^{-3}	[44]
Hamaker-constant graphite-graphite	4.64 • 10^{-20} J	[69]
Thickness of polymer layer on the graphite particles	39 nm	Calculated based on [47]
Specific volume solvent	1.0873 nm^3	Calculated based on [47]
Molecular weight CMC	2.24• 10^5 g mol^{-1}	[71]

Table A4
Film thickness at roll gap, stress at roll gap and final film thickness resulting from calendaring simulations.

Calendering Degree	Film thickness at roll gap / μm		Stresses at roll gap / MPa	
	Simulation	Experiment	Simulation	Experiment
7.6 mg cm^{-2}				
1	62.25 ± 0.0403	63.22 ± 0.89	1.18 ± 0.0047	1.17 ± 0.65
2	57.96 ± 0.0602	53.41 ± 0.05	1.84 ± 0.0094	1.83 ± 0.41
3	48.79 ± 0.1636	44.11 ± 0.17	4.39 ± 0.0141	4.37 ± 1.23
4	35.34 ± 0.1266	36.71 ± 1.00	13.81 ± 0.0205	13.76 ± 0.83
9.2 mg cm^{-2}				
1	83.05 ± 0.4229	78.11 ± 0.06	0.55 ± 0.0000	0.55 ± 0.57
2	63.89 ± 0.1417	63.81 ± 0.16	2.86 ± 0.0000	2.84 ± 1.23
3	50.69 ± 0.6941	50.38 ± 0.21	8.16 ± 0.0170	8.11 ± 1.56
4	38.86 ± 0.0665	45.07 ± 0.38	17.97 ± 0.0852	17.79 ± 1.16
11.3 mg cm^{-2}				
1	87.48 ± 0.2368	88.16 ± 0.14	1.37 ± 0.0047	1.35 ± 0.45
2	74.12 ± 0.0634	73.91 ± 0.30	3.43 ± 0.0094	3.39 ± 0.82
3	67.56 ± 0.0490	66.67 ± 0.38	5.31 ± 0.0047	5.25 ± 0.94
4	52.26 ± 0.1109	61.79 ± 0.29	13.53 ± 0.0205	13.40 ± 0.78
14.3 mg cm^{-2}				
1	84.18 ± 0.0125	99.54 ± 0.05	3.79 ± 0.0262	5.44 ± 0.12
2	70.92 ± 0.0330	86.13 ± 0.20	7.49 ± 0.0909	10.66 ± 0.49
3	59.13 ± 0.0386	73.83 ± 0.61	12.69 ± 0.0464	18.22 ± 1.36
4	38.64 ± 0.0450	64.82 ± 0.29	25.77 ± 0.0946	35.54 ± 0.64

Calendering Degree	Final layer thickness / μm	
	Simulation	Experiment
7.6 mg cm^{-2}		
1	67.59 ± 0.3873	73.50 ± 0.52
2	64.53 ± 0.1586	65.33 ± 0.63
3	59.90 ± 0.2355	59.67 ± 0.98
4	56.16 ± 0.1247	52.33 ± 0.55
9.2 mg cm^{-2}		
1	86.30 ± 0.5546	86.50 ± 0.55
2	73.63 ± 0.3685	77.00 ± 0.89
3	68.78 ± 0.9216	66.67 ± 0.52
4	67.08 ± 0.7213	60.83 ± 0.63
11.3 mg cm^{-2}		
1	93.70 ± 0.1837	99.93 ± 0.52
2	86.76 ± 0.3301	89.33 ± 0.82
3	84.00 ± 0.3171	83.00 ± 0.55
4	80.77 ± 0.9476	75.5 ± 0.63
14.3 mg cm^{-2}		

(*continued on next page*)

Table A4 (*continued*)

Calendering Degree	Final layer thickness / µm	
	Simulation	Experiment
1	103.93 ± 0.3504	117.5 ± 0.55
2	101.00 ± 0.5802	100.67 ± 0.82
3	100.02 ± 0.2428	91.17 ± 0.75
4	96.23 ± 0.4692	82.33 ± 0.52

Data availability

Data will be made available on request.

References

[1] McKinsey, Battery 2030: Resilient, sustainable, and circular. Battery demand is growing—and so is the need for better solutions along the value chain, 2023.
[2] A. Kwade, W. Haselrieder, R. Leithoff, A. Modlinger, F. Dietrich, K. Droeder, Nat. Energy 3 (2018) 290–300.
[3] M. Müller, L. Pfaffmann, S. Jaiser, M. Baunach, V. Trouillet, F. Scheiba, P. Scharfer, W. Schabel, W. Bauer, J. Power Sources 340 (2017) 1–5.
[4] N. Kumano, Y. Yamaguchi, Y. Akimoto, A. Ohshima, H. Nakamura, M. Yamamura, J. Power Sources 591 (2024) 233883.
[5] H. Dreger, W. Haselrieder, A. Kwade, J. Energy Storage 21 (2019) 231–240.
[6] W. Haselrieder, S. Ivanov, D.K. Christen, H. Bockholt, A. Kwade, ECS Trans. 50 (2013) 59–70.
[7] C. Meyer, M. Weyhe, W. Haselrieder, A. Kwade, Energy Tech. (2020) 8.
[8] W. Haselrieder, B. Westphal, H. Bockholt, A. Diener, S. Höft, A. Kwade, Int. J. Adhes. Adhes. 60 (2015) 1–8.
[9] S. Scheffler, R. Jagau, N. Müller, A. Diener, A. Kwade, Batteries 8 (2022) 46.
[10] M. Abdollahifar, H. Cavers, S. Scheffler, A. Diener, M. Lippke, A. Kwade, Adv. Energy Mater. (2023) 13.
[11] I. Srivastava, D.S. Bolintineanu, J.B. Lechman, S.A. Roberts, ACS Appl. Mater. Interfaces 12 (2020) 34919–34930.
[12] T. Lombardo, J.-B. Hoock, E.N. Primo, A.C. Ngandjong, M. Duquesnoy, A. A. Franco, Batter. Supercaps 3 (2020) 721–730.
[13] T. Lombardo, A.C. Ngandjong, A. Belhcen, A.A. Franco, Energy Storage Mater. 43 (2021) 337–347.
[14] T. Lombardo, F. Lambert, R. Russo, F.M. Zanotto, C. Frayret, G. Toussaint, P. Stevens, M. Becuwe, A.A. Franco, Batter. Supercaps (2022) 5.
[15] M. Lippke, T. Ohnimus, F. Frankenberg, C. Schilde, A. Kwade, Powder Technol. 444 (2024) 119984.
[16] J. Kumberg, M. Baunach, J.C. Eser, A. Altvater, P. Scharfer, W. Schabel, Energy Tech. (2021) 9.
[17] J. Kumberg, M. Baunach, J.C. Eser, A. Altvater, P. Scharfer, W. Schabel, Energy Tech. (2021) 9.
[18] F. Font, B. Protas, G. Richardson, J.M. Foster, J. Power Sources 393 (2018) 177–185.
[19] C. Zihrul, M. Lippke, A. Kwade, Batteries 9 (2023) 455.
[20] D. Schreiner, J. Lindenblatt, R. Daub, G. Reinhart, Energy Tech. (2023) 11.
[21] D.O. Potyondy, P.A. Cundall, Int. J. Rock Mech. Min. Sci. 41 (2004) 1329–1364.
[22] S.C. Thakur, J.P. Morrissey, J. Sun, J.F. Chen, J.Y. Ooi, Granul. Matter 16 (2014) 383–400.
[23] A.C. Ngandjong, T. Lombardo, E.N. Primo, M. Chouchane, A. Shodiev, O. Arcelus, A.A. Franco, J. Power Sources 485 (2021) 229320.
[24] C. Sangrós Giménez, B. Finke, C. Nowak, C. Schilde, A. Kwade, Adv. Powder Technol. 29 (2018) 2312–2321.
[25] C. Sangrós Giménez, B. Finke, C. Schilde, L. Froböse, A. Kwade, Powder Technol. 349 (2019) 1–11.
[26] Colin Thornton, Zemin Ning, Powder Technol. (1998) 154–162.
[27] C. Thornton, J. Appl. Mech. (1997) 383–386.
[28] D. Weitze, F.M. Zanotto, D.Z. Dominguez, A.A. Franco, Energy Storage Mater. 73 (2024) 103747.
[29] J. Xu, B. Paredes-Goyes, Z. Su, M. Scheel, T. Weitkamp, A. Demortière, A.A. Franco, Batter. Supercaps (2023) 6.
[30] A. Diener, S. Ivanov, W. Haselrieder, A. Kwade, Energy Tech. (2022) 10.
[31] C. Meyer, H. Bockholt, W. Haselrieder, A. Kwade, J. Mater. Process. Technol. 249 (2017) 172–178.
[32] M. Lippke, T. Ohnimus, T. Heckmann, D. Ivanov, P. Scharfer, W. Schabel, C. Schilde, A. Kwade, Energy Tech. (2023) 11.
[33] J. Klemens, L. Schneider, E.C. Herbst, N. Bohn, M. Müller, W. Bauer, P. Scharfer, W. Schabel, Energy Tech. (2022) 10.
[34] J. Klemens, L. Schneider, D. Burger, N. Zimmerer, M. Müller, W. Bauer, H. Ehrenberg, P. Scharfer, W. Schabel, Energy Tech. (2023) 11.
[35] A. Altvater, J. Klemens, J. Borho, A. Smith, T. Heckmann, P. Scharfer, W. Schabel, Energy Tech 12 (2024).
[36] A. Altvater, T. Heckmann, J.C. Eser, S. Spiegel, P. Scharfer, W. Schabel, Energy Tech. (2023) 11.
[37] E.-U. Schlünder, Dry. Technol. 22 (2004) 1517–1532.
[38] J. Kumberg, M. Müller, R. Diehm, S. Spiegel, C. Wachsmann, W. Bauer, P. Scharfer, W. Schabel, Energy Tech. (2019) 7.
[39] J.C. Eser, T. Wirsching, P.G. Weidler, A. Altvater, T. Börnhorst, J. Kumberg, G. Schöne, M. Müller, P. Scharfer, W. Schabel, Energy Tech. (2020) 8.
[40] VDI-Buch, Springer Vieweg, Berlin, 2013.
[41] H. Luo, C.M. Cardinal, L.E. Scriven, L.F. Francis, Langmuir ACS J. Surf. Coll. 24 (2008) 5552–5561.
[42] S. Lim, K.H. Ahn, M. Yamamura, Langmuir 29 (2013) 8233–8244.
[43] S. Jaiser, J. Kumberg, J. Klaver, J.L. Urai, W. Schabel, J. Schmatz, P. Scharfer, J. Power Sources 345 (2017) 97–107.
[44] DDBST - DDBST GmbH, can be found under, https://www.ddbst.com/, 2024.
[45] J.H. Park, S.H. Kim, K.H. Ahn, Colloids Surf. A Physicochem. Eng. Asp. 664 (2023) 131130.
[46] C.D. Reynolds, S.D. Hare, P.R. Slater, M.J.H. Simmons, E. Kendrick, Energy Tech. (2022) 10.
[47] F. Ma, Y. Fu, V. Battaglia, R. Prasher, J. Power Sources 438 (2019) 226994.
[48] T. Breinlinger, T. Kraft, Powder Technol. 256 (2014) 279–284.
[49] D. Schreiner, J. Lindenblatt, F.J. Günter, G. Reinhart, Procedia CIRP 104 (2021) 91–97.
[50] S. Jaiser, A. Friske, M. Baunach, P. Scharfer, W. Schabel, Dry. Technol. 35 (2017) 1266–1275.
[51] B. Westphal, H. Bockholt, T. Günther, W. Haselrieder, A. Kwade, ECS Trans. 64 (2015) 57–68.
[52] Clara Sangrós Giménez, DEM-based modelling of the structural, mechanical and electrical behaviour of lithium-ion battery electrodes, Dissertation, 2020.
[53] M. Weber, A. Schoo, M. Sander, J.K. Mayer, A. Kwade, Energy Tech. (2023) 11.
[54] M. Lippke, T. Ohnimus, T. Heckmann, D. Ivanov, P. Scharfer, W. Schabel, C. Schilde, A. Kwade, Energy Tech. (2023) 11.
[55] S. Jaiser, N. Sanchez Salach, M. Baunach, P. Scharfer, W. Schabel, Dry. Technol. 35 (2017) 1807–1817.
[56] F.L.E. Usseglio-Viretta, A. Colclasure, A.N. Mistry, K.P.Y. Claver, F. Pouraghajan, D.P. Finegan, T.M.M. Heenan, D. Abraham, P.P. Mukherjee, D. Wheeler, et al., J. Electrochem. Soc. 165 (2018) A3403–A3426.
[57] V. Arumughan, T. Nypelö, M. Hasani, H. Brelid, S. Albertsson, L. Wågberg, A. Larsson, Colloids Surf. A Physicochem. Eng. Asp. 626 (2021) 127006.
[58] V. Arumughan, T. Nypelö, M. Hasani, A. Larsson, Biomacromolecules 23 (2022) 47–56.
[59] H. Hagiwara, W.J. Suszynski, L.F. Francis, J. Coat. Technol. Res. 11 (2014) 11–17.
[60] L. Pfaffmann, S. Jaiser, M. Müller, P. Scharfer, W. Schabel, W. Bauer, F. Scheiba, H. Ehrenberg, J. Power Sources 363 (2017) 460–469.
[61] T. Oku, M. Eto, Nucl. Eng. Des. (1992) 239–243.
[62] E. Solfiti, F. Berto, Procedia Struct. Integrity 25 (2020) 420–429.
[63] H. Zimmermann 1994.
[64] J.B. Spicer, F.W. Zeng, K. Han, L.R. Olasov, N.C. Gallego, C. I. Contescu in 2014 IEEE International Ultrasonics Symposium, IEEE, 2014, pp. 232–235.
[65] R. Ge, D.J. Cumming, R.M. Smith, Powder Technol. 403 (2022) 117366.
[66] K. M, F. V, M. J, C. A, Adv. Mater. Sci. (2018) 3.
[67] K. Giannis, C. Thon, G. Yang, A. Kwade, C. Schilde, Powder Technol. 432 (2024) 119122.
[68] T. Lokajicek, P. Lukas, A.N. Nikitin, I.V. Papushkin, V.V. Sumin, R.N. Vasin, Carbon 49 (2011) 1374–1384.
[69] M. Zhu, J. Park, A.M. Sastry, J. Electrochem. Soc. 158 (2011) A1155.
[70] J. Cho, J.J. Luo, I.M. Daniel, Compos. Sci. Technol. 67 (2007) 2399–2407.
[71] T. Sugama, T. Pyatina, Cem. Concr. Compos. 55 (2015) 281–289.